Ocean Engineering 310 (2024) 118670

Contents lists available at ScienceDirect

Ocean Engineering

journal homepage: www.elsevier.com/locate/oceaneng

Research paper

Full-scale measurements and analysis of the floating installation of an offshore wind turbine tower

David Fidalgo Domingos [a,b], Panagiota Atzampou [c], Peter Christiaan Meijers [d], Sebastião Holbeche Beirão [e], Andrei V. Metrikine [c,d], Jan-Willem van Wingerden [a], Peter Wellens [b,*]

[a] Delft Center for Systems and Control, Delft University of Technology, Mekelweg 2, Delft, 2628 CD, The Netherlands
[b] Maritime and Transport Technology, Delft University of Technology, Mekelweg 2, Delft, 2628 CD, The Netherlands
[c] Department of Engineering Structures, Delft University of Technology, Stevinweg 1, Delft, 2628 CN, The Netherlands
[d] Department of Hydraulic Engineering, Delft University of Technology, Stevinweg 1, Delft, 2628 CN, The Netherlands
[e] Técnico Solar Boat, Instituto Superior Técnico, Avenida Rovisco Pais 1, Lisbon, 1049-001, Portugal

ARTICLE INFO

Keywords:
Offshore wind turbines
Floating installation
Full-scale measurements
VIV
AHRS
Tugger lines

ABSTRACT

Europe has set an ambitious target to increase the offshore wind power capacity to approximately 30 GW by 2026. With nearshore locations already allocated, future wind farms must be installed in deeper waters, pushing the operational limits of currently used jack-up vessels. Utilizing existing floating heavy-lift vessels presents a viable alternative. This paper disseminates data gathered during the full-scale testing campaign of a floating installation of an offshore wind turbine tower. For this purpose, novel time-synchronized motion-tracking units were developed. Analysis of the obtained data reveals that approximately 96% of the motion response of the tower is due to wave action and 3% to vortex-induced vibrations caused by the presence of a passive tugger line, which shifted one of the system's natural frequencies towards the tower's vortex-shedding frequency. Next to wind and wave-induced motion, the data reveal that the hoisting itself induces tower vibrations, accounting for less than 1% of the tower motion response. The collected data offer a distinctive perspective on this type of installation, which is unlikely to be replicated at model scale due to the scaling limitations associated with the interdependence of waves and wind. The data can be used to validate motion control strategies to enhance the efficiency, safety, and workability of floating offshore wind turbine installations.

1. Introduction

Driven by the effects of climate change, the global energy sector is undergoing a transition from fossil fuels as main sources of energy to renewable energy. As a result, investments in wind energy have surged in recent decades (Bilgili and Alphan, 2022). As a result of more stable wind conditions and the depletion of onshore and nearshore locations, wind farms are moving further offshore, into deeper waters, Domingos et al. (2023), Ramirez et al. (2019). According to a recent Wind Europe report (WindEurope, 2022), Europe has set the ambitious goal of installing 116 GW of additional wind turbines by 2025, one-fourth of which offshore wind turbines (OWTs). To meet this goal and satisfy ever-increasing energy demands, OWTs with greater capacities and thus bigger dimensions are being installed in deeper waters (Díaz and Soares, 2020). Over the years, jack-up vessels have monopolized the installation of OWTs worldwide. As these vessels are constrained by their installation depth and lifting capacity (Zhao et al., 2019), an opportunity arises for heavy lift vessels (HLVs). Traditionally used in the oil and gas industry, HLVs can lift loads up to 20,000 tonnes, and as such appear well-suited for the deployment of heavy wind turbine assemblies at water depths beyond the limits of jackup vessels (Jiang, 2021). Another issue with installing large OWTs is the sensitivity of the operation to wind direction changes (wind veering). The dynamic positioning system (DP) has the potential to reduce this sensitivity, at the price of increasing the sensitivity to wave loading (Ku and Roh, 2015; Cha et al., 2010). The latter external excitation is of primary importance to payload motion (Cha et al., 2010; Ren et al., 2021), limiting workability (Domingos et al., 2023).

The project 'Floating installation Offshore XXL wind turbines' (DOT6000-FOX) was funded by the Netherlands Enterprise Agency RVO to study the cost-effectiveness of HLVs for the installation of OWTs compared to current methods, towards broadening the industry's installation options. During the offshore campaign (October 2021), a 2.75

* Corresponding author.
E-mail address: p.r.wellens@tudelft.nl (P. Wellens).

https://doi.org/10.1016/j.oceaneng.2024.118670
Received 28 March 2024; Received in revised form 27 June 2024; Accepted 3 July 2024
Available online 24 July 2024

Fig. 1. Semi-submersible crane vessel Sleipnir of Heerema Marine Contractors performing a floating offshore installation of an OWT (DOB-Academy, 2022).

MW OWT was installed, see Fig. 1. The consortium of the DOT6000-FOX project consists of Delft Offshore Turbine B.V. (DOT), responsible for the OWT; Heerema Marine Contractors Nederland SE (HMC), which employed Sleipnir, the largest semi-submersible HLV to date; and Delft University of Technology (TU Delft), which developed tailored sensors to record the motion of the wind turbine components during various stages of the offshore campaign. These sensors offer the significant advantage of synchronization with any onboard measurement system in Coordinated Universal Time (UTC).

Scaling limitations pose challenges in reproducing offshore operations at model-scale. On one hand, wind loads are a function of the ratio between inertial and viscous forces, which scales proportionally with the geometric scaling factor (λ) (*Reynolds number scaling*). On the other hand, wave loads are a function of the ratio between inertial and gravitational forces, which scales with the inverse of the square root of λ (*Froude number scaling*). This scaling inconsistency is often referred as "The Dilemma in Model Testing" (Larsson, 2010). Furthermore, mathematical models, as well as reduced-scale models are often simplified, which can condition the outcomes. This work aims at complementing the existing literature by providing an analysis of the full-scale dynamics of an OWT tower installation using a floating vessel and corresponding data. The response of the crane-payload-vessel dynamical system is examined and discussed alongside an analysis of the effects of environmental disturbances. Moreover, the collected sensor data from the attitude and heading reference system (AHRS) deployed offshore, is made publicly available with this article (Domingos et al., 2024) in order to support the reproducibility of results, the validation of numerical models, and the development of novel motion control strategies, Meskers and van Dijk (2012), Atzampou et al. (2024).

The paper is organized as follows: The dynamical system of the operation, the development and placement of sensors in the full-scale testing campaign, and the methodology employed for data treatment are presented in Section 2. The numerical model analysis is presented in Section 3. Section 4 details the findings and analysis of the measurements and the system's response. Lastly, Section 5 draws conclusions and offers recommendations for future work.

Table 1
Overview of the system parameters.

Parameter	Notation	Value	Unit
Crane Tip Height[a]	H_k	180	m
Tower Height	L_c	74	m
Averaged Tower Diameter	d_T	3.6	m
Tower Mass	M	226	ton
Block Mass	m	45	ton
Sling Length	ℓ_s	10.6	m
Passive Tugger Length	L_{PT}	2×10^1	m
Passive Tugger Diameter	d_{PT}	0.064	m
Passive Tugger Young's Modulus[b]	E_{PT}	113	GPa

[a] With respect to waterline.
[b] Three stranded polypropylene rope.

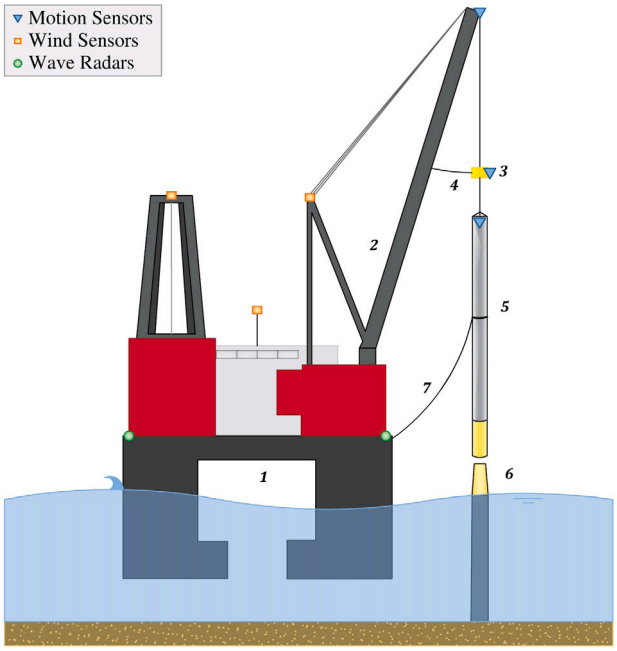

Fig. 2. Schematic diagram of the tower installation: 1. Floating vessel, 2. Heavy lift crane, 3. Lifting block/hook, 4. Active (damping) tugger line, 5. Wind turbine tower, 6. Monopile head and 7. Passive (manual) tugger line. Symbols indicate motion sensors, wind sensors, and wave radars.

2. Methodology

2.1. Description of the dynamical system

This study concerns the set-down stage of the OWT installation, during which the tower is suspended by the crane and lowered towards the monopile foundation. A schematic representation of this operation is presented in Fig. 2. Fundamentally, the system comprises the floating crane vessel and the suspended load subsystem that resembles a triple pendulum. The constituent elements of this triple pendulum are the crane cable and block hook, as well as the sling linking the hook to the attachment point of the suspended load. This load corresponds to a hollow cylindrical structure representing the OWT tower. The numerical values for the parameters of this system are listed in Table 1.

To compensate for the external disturbances originating from wind and waves, two tugger line systems were deployed (Fig. 3). An active tugger line is attached to the hook block to damp out its motion and thus constrain the vibrations of the suspended tower. In addition, a set of passive tugger lines was directly connected to the tower above its center of gravity (Fig. 2). The latter tugger line system was connected to a cleat and manually operated by the crew.

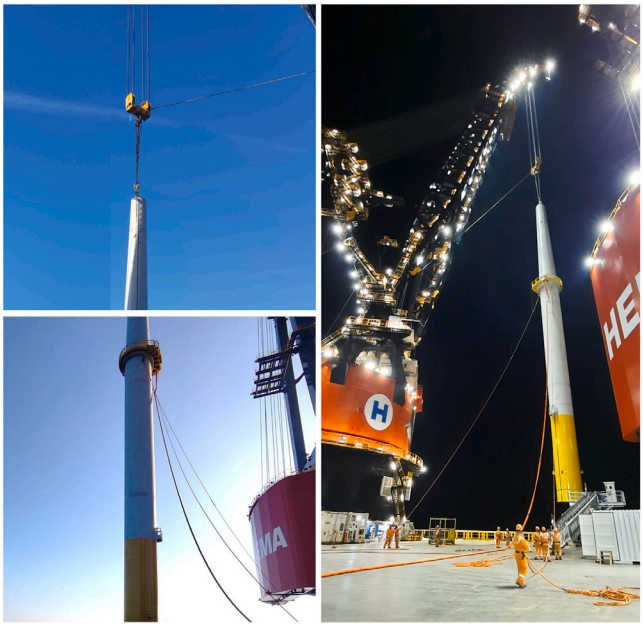

Fig. 3. Tugger lines attached to the OWT tower during installation: Active tugger line attached on the hook block (top left), passive manual tugger line attached on the skybox location on the lower tower (lower left), and overview picture (right). Sensor locations are detailed in Fig. 2.

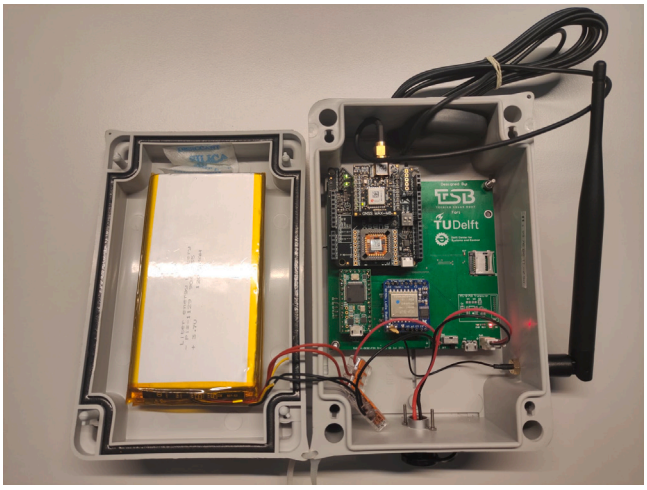

Fig. 4. Wireless motion tracking module.

2.2. Sensors design and placement

Since only part of the required data, *e.g.* wave motion and tugger line loads, are recorded by the vessel's on-board monitoring system, the offshore measurement campaign required the development of tailored motion tracking units, as shown in Fig. 4. These units were designed to

- withstand challenging environmental conditions and mechanical loads;
- be deployed at locations that were difficult to access;
- be operated with five days of autonomy;
- synchronize the data to UTC;
- facilitate both real-time data transmission and local data storage.

The units were designed and developed in partnership with the Técnico Solar Boat (TSB) team from the Instituto Superior Técnico in Portugal. They consisted of an AHRS *Xsens MTi-7* GNSS/INS sensor for motion measurements, a *Teensy* microprocessor responsible for reading and locally saving measurements on a micro SD-card, as well as for transmitting them to a receiver station using a *LoRa* radio transceiver. Power was supplied by two 12 Ah Li-Po batteries. The printed circuit board (PCB), designed by TSB, interconnected all subsystems and monitored the batteries' health. The specifications of the AHRS's accelerometer and gyroscope measurements are described in Table 2.

Table 2
Sensor specifications.

Sensor	Bias	Noise	Sampling rate
AHRS accelerometer	40 μg	70 $\mu g/\sqrt{Hz}$	5 Hz
AHRS gyroscope	6 deg/h	$3 \cdot 10^{-3} deg\ s^{-1}/\sqrt{Hz}$	5 Hz

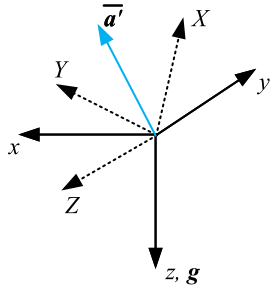

Fig. 5. Reference frames used for processing the raw acceleration and angular velocity data. Global reference frame xyz, local reference frame XYZ, normalized mean acceleration vector $\overline{\mathbf{a}'}$, and preferred direction of gravitational acceleration $\mathbf{g}$.

Wind, wave, and tugger line loads as well as hoisting cable length data were measured during the campaign by an array of radars and sensors, which were strategically located on the vessel as shown in Fig. 2. More specifically, wind speeds were measured using anemometers at the top of the cranes' A-brackets and on the met-mast on top of the super-structure. The actual wind speed was estimated from the wind measurements at these points. The sea state was measured using two wave radars, on the starboard and portside of the vessel. The motion measurements were performed using the motion tracking modules presented in Fig. 4. The sampling rate of the wind sensors, wave radars, tugger gauges, and hoisting cable encoder was 1 Hz, time synchronized to UTC. For these measurements, the sensors' noise level and bias are not available.

2.3. Data treatment

Each sensor unit measured the raw acceleration and angular velocity in its local frame of reference, which is denoted by XYZ, see Fig. 5. This data is publicly available in Domingos et al. (2024). Normally, in an AHRS, these motion components are transformed to an Earth-fixed reference frame using GNSS. Here, instead, the raw acceleration and angular velocity data are transformed in post-processing such that the measured mean acceleration vector always aligns with the positive z-axis of the global xyz-frame. This transformation ensures that the gravitational acceleration points along the z-axis regardless of the sensor unit's orientation.

In the local XYZ reference frame, the sensor measures the acceleration $\mathbf{a}'(t)$ and angular velocity $\mathbf{\Omega}'(t)$, where the prime denotes the quantity in the local frame. By applying the time-invariant rotation matrix $\mathbf{R}$ to the time signals, the acceleration $\mathbf{a}(t)$ and angular velocity $\mathbf{\Omega}(t)$ become

$$\mathbf{a}(t) = \mathbf{R}\mathbf{a}'(t), \tag{1}$$

$$\mathbf{\Omega}(t) = \mathbf{R}\mathbf{\Omega}'(t). \tag{2}$$

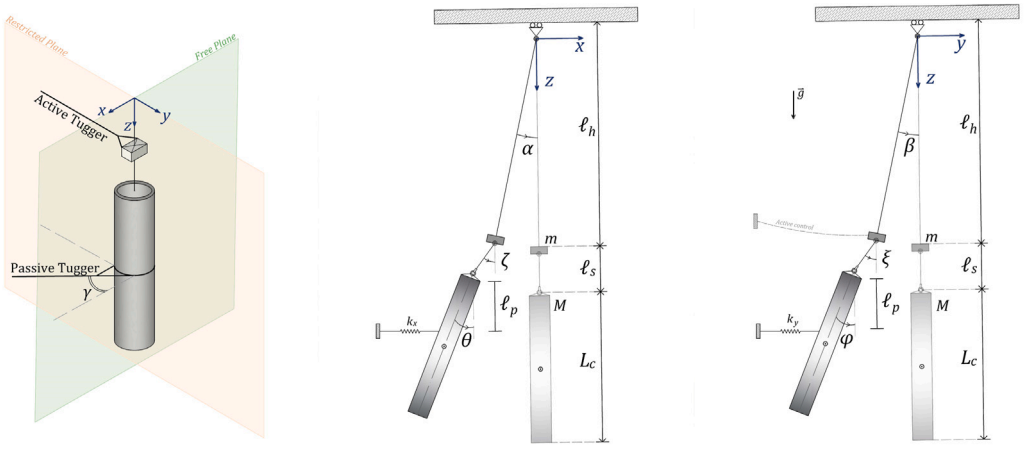

(a) Active and passive tugger line orientation. (b) *xz*-plane (free) (c) *yz*-plane (restrained)

Fig. 6. Schematics of the numerically simulated triple spherical pendulum system analogue.

The rotation matrix **R** ensures that the normalized mean acceleration vector $\overline{\mathbf{a}'}$ aligns with the preferred direction of gravitational acceleration, which is denoted by the unit vector **g** in Fig. 5. Using a variant of Rodrigues' rotation formula (Cis and Tojo, 2018), the rotation matrix **R** is given by

$$\mathbf{R} = \mathbf{I} + \mathbf{K} + \frac{1}{1 + \overline{\mathbf{a}'} \cdot \mathbf{g}} \mathbf{K}^2, \tag{3}$$

where **I** is the identity matrix, $(\cdot)$ represents the inner product, and **K** is

$$\mathbf{K} = \mathbf{g} \otimes \overline{\mathbf{a}'} - \overline{\mathbf{a}'} \otimes \mathbf{g}, \tag{4}$$

in which $(\otimes)$ denotes the outer product.

After rotation, the acceleration components a_x and a_y are in the plane perpendicular to **g**, and Ω_z describes the angular velocity about the *z*-axis. Note that the exact orientations of the *x*- and *y*-axes are not defined by this rotation operation. However, since our main interest is to quantify and identify the cause for the motion of OWT components in the plane parallel to the sea surface, the exact orientation of these axes is less important. In the remainder, components a_x and a_y will be referred to as the in-plane accelerations.

3. Dynamics of the crane-payload-tugger system

To estimate the natural frequencies of the full-scale system, a simplified mathematical model is used. This model comprises a suspended cylinder of mass M (and a uniform diameter along its length) to represent the tower, and a point mass (m) pendulum representing the hook block and main crane cable (ℓ_h). These two subsystems are connected through a rigid rod simulating the sling (ℓ_s). The resulting triple pendulum is free to oscillate in 3D space and its motion is projected into two perpendicular planes: *xz*- and *yz*-plane, see Fig. 6.

The motion of the system is restrained by the use of tugger lines. In Fig. 6(a), the spatial tugger line placement is presented alongside the orientation of the axes selected as the frame of reference for this model. In contrast with the active tugger attached to the hook block, the passive line is rigidly attached to the vessel deck by means of a cleat. Consequently, this tugger influences the dynamics of the suspended system. Given that it is pre-tensioned, for small motion amplitudes it can be modeled as a linear spring element (de Kruif and Rossin, 2021) connecting the vessel's deck to the tower, at a distance $\ell_p = 31$ m from its suspension point, see Fig. 6. As the passive tuggers are oriented at an angle γ with respect to the two planes, the force exerted by this spring is projected onto two components (with spring coefficients k_x and k_y, respectively) in the *xz*- and *yz*-planes to account for its out-of-plane orientation. The complete derivation of the equations of motion of the dynamical system is detailed in Appendix A.

Since the motion of the system is not actively controlled in the *xz*-plane, it is reasonable to derive the modes of the system by studying only the planar triple pendulum with a spring k_x (Fig. 6(b)). The forces exerted by the passive tugger lines were not recorded throughout the operation. Furthermore, the exact orientation of the tugger is not known. Thus, the natural frequencies of the system are calculated as a function of the spring coefficient k_x (for $\gamma = 0°$) as shown in Fig. 7(a). The influence of the stiff spring is evident when $k_x > 10^4$, thus increasing the natural frequencies, especially in the second and third modes. The values of the natural frequencies of the system with (highly restrained system, $k_x = 10^6$ N/m) and without (free system, $k_x = 0$ N/m) a passive tugger line are given in Table 3.

Table 3
Natural frequencies per mode of vibration.

Modes	$k_x = 0$ N/m	$k_x = 10^6$ N/m	$k_x = 2.14 \cdot 10^5$ N/m
Mode 1 [Hz]	$f_{n,1} = 0.048$	$f_{n,1} = 0.094$	$f_{n,1} = 0.087$
Mode 2 [Hz]	$f_{n,2} = 0.112$	$f_{n,2} = 0.332$	$f_{n,2} = 0.166$
Mode 3 [Hz]	$f_{n,3} = 0.446$	$f_{n,3} = 0.918$	$f_{n,3} = 0.581$

The axial stiffness of the passive tugger can be estimated by utilizing the known characteristics of the ropes provided in Table 1, as follows:

$$k_{PT} = \frac{E_{PT} A_{PT}}{L_{PT}} = 2.14 \cdot 10^5 \text{ N/m}. \tag{5}$$

Evaluating the model with the stiffness k_{PT} for $\gamma = 0°$, the following values for the natural frequencies are derived: for Mode 1: $f_{n,1} = 0.087$ Hz, for Mode 2: $f_{n,2} = 0.166$ Hz and for Mode 3: $f_{n,3} = 0.581$ Hz (Table 3). It is anticipated that these values might be slightly lower due to the out-of-plane orientation of the tugger ($\gamma > 0°$) and the fact that the connection of the tugger to the cleat is not perfectly stiff. Fig. 7(b) presents the decrease in the effective spring coefficient k_x (for the estimated stiffness k_{PT}) for different angles γ as well as the corresponding values of the natural frequencies of the three modes. A small decrease occurs in the natural frequency of the second and third modes when $\gamma > 20°$.

Once aligned with the monopile foundation, the tower is progressively lowered (with intervals of constant length). The time series of the main cable payout length (ℓ_h) during the two lifts studied is shown in Fig. 8. To assess the effect of the changes in payout length (l_h) on the dynamic behavior of the system, an analysis was performed using the frequency-domain framework presented by Domingos et al. (2023). The results shown in Fig. 9 are in accordance with the natural frequencies

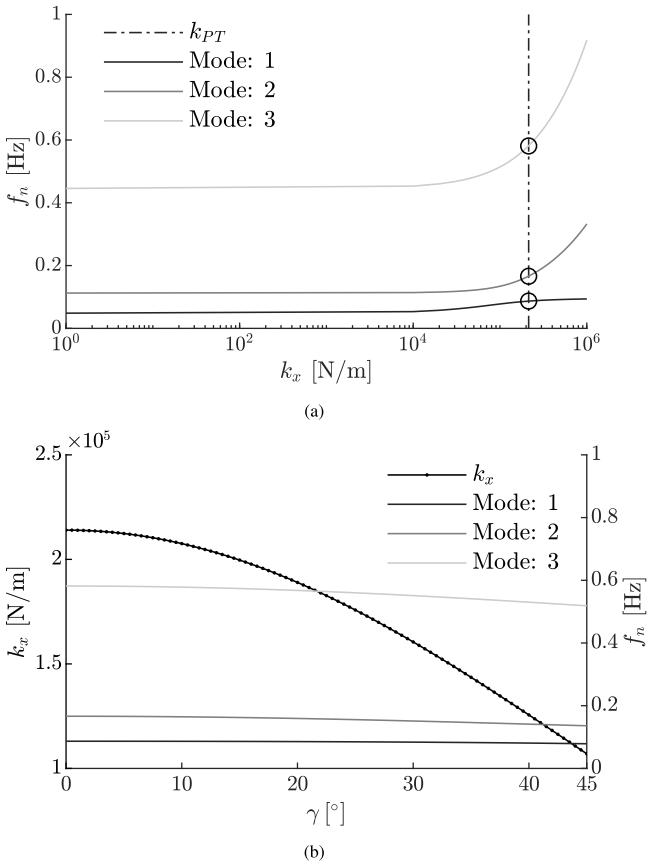

Fig. 7. (a) Natural frequencies for different stiffness coefficients k_x and $\gamma = 0°$. (b) Stiffness k_x (left vertical axis) and corresponding natural frequency f_n (right vertical axis) for estimated tugger stiffness k_{PT} and different orientation angles γ.

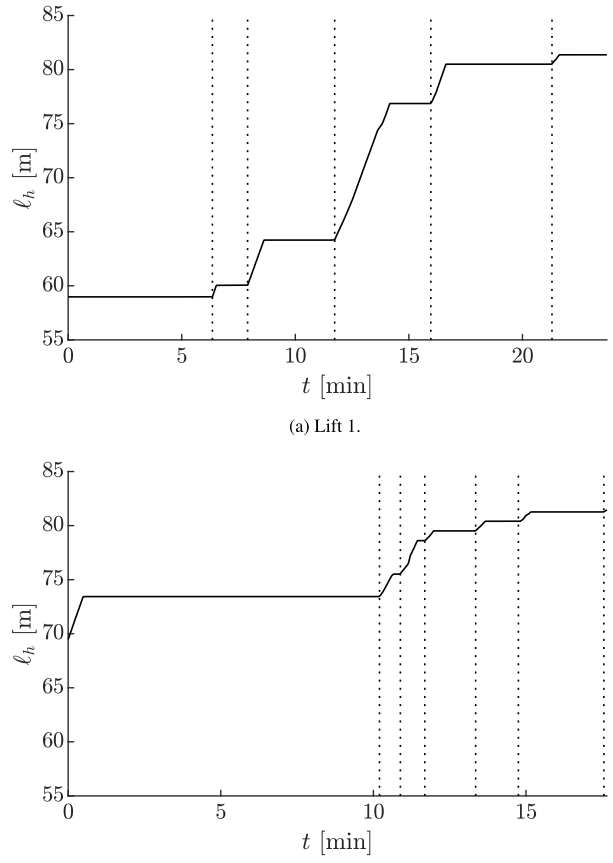

Fig. 8. Payout length as a function of time during tower installation.

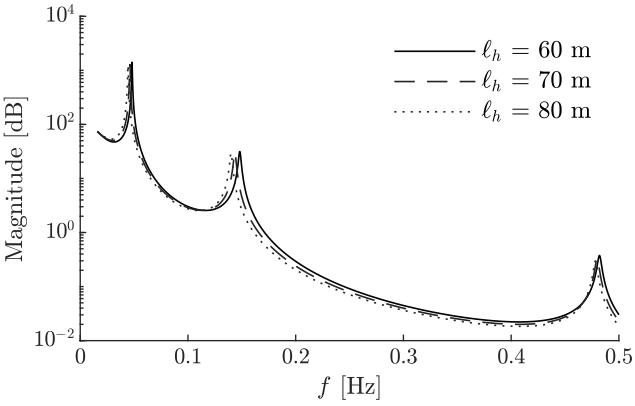

Fig. 9. Unrestrained tower motion response to crane tip accelerations for different payout lengths.

presented in Table 3 for the unrestrained case. Moreover, the recorded changes in the payout length have limited influence on the dynamic response of the system.

4. Data analysis and discussion

The operation analyzed in this work is the lowering of an OWT tower on a pre-installed monopile using a semi-submersible crane vessel (Fig. 2). During the lowering, the crane's orientation and boom angle were kept constant; the only parameter that varied was the hoisting length as the tower was lowered towards the monopile. Datasets from two separate lifts are studied and compared to gain insight into the influence of different external environmental excitations and lowering speeds on the response of the overall dynamical system.

For the in-plane motion of the two components of the tower-block system, the power density spectra are analyzed to identify the frequency range contributing most significantly to the tower's motions. Subsequent time–frequency analysis delves into the time variance of the energy to identify the modes of vibration as well as the physical processes exciting these modes. One of the processes, wind-induced vibrations, is discussed in more depth. Lastly, in Section 4.4, the contribution of these disturbances to the actual motion of the components is analyzed.

4.1. Power density spectra of the in-plane acceleration

Fig. 10 presents the power density spectra (PDS) of the in-plane accelerations of the different components of the system as well as the energy density measured by the wave radars for Lift 1 and 2. It is noted that the tugger line tension has a non-zero mean, which is attributed to the variation in tugger tension set-point during the operation. By comparing the wave energy spectra of the portside (PS) and starboard (SB) wave radars for Lift 1 and Lift 2, it is clear that the sea state was calmer during Lift 2 than during Lift 1. The peak period T_p and significant wave height H_s are determined from these uni-directional spectra as follows: $T_p = 12.2$ s and $H_s = 0.45$ m for Lift 1 and $T_p = 13.5$ s and $H_s = 0.30$ m for Lift 2. These values suggest that the two operations were conducted under calm sea conditions.

The crane tip, hook block, and upper tower acceleration spectra have a common acceleration peak at approximately 0.09 Hz for both lifts (Fig. 10). This peak matches the data from the wave radars,

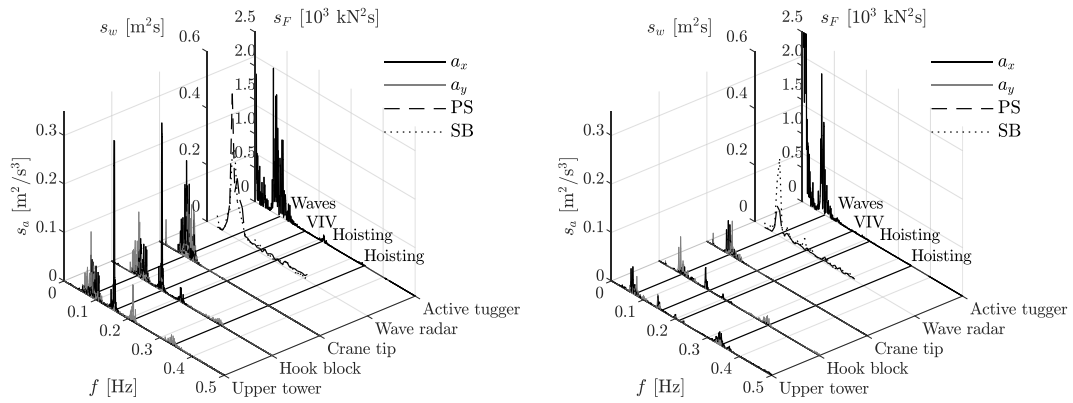

(a) Lift 1. (b) Lift 2.

Fig. 10. Power density spectra for the in-plane accelerations, the wave radar, and the active tugger line force as measured during Lift 1 and Lift 2. The translational accelerations in the xy plane are denoted as a_x and a_y for the x- and $y$axis, respectively. The abbreviations PS and SB denote the port side and starboard side of the vessel, respectively. The acceleration power density spectra uncertainty is of the order $\mathcal{O}(10^{-4})$, Fig. C.15. For the remaining measurements, sensor bias and noise are not available.

suggesting that, at this frequency, wave energy is effectively being transferred to the block-tower system through the crane tip. Note that the motion sensors have a higher sampling rate than the wave radars, resulting in a higher resolution of the acceleration spectra. Naturally, the energy associated with the crane tip motion of Lift 1 is higher than Lift 2, due to the higher wave energy density of the former.

The crane tip sensor detected only one acceleration peak frequency, matching the range of wave energy measured by the wave radars. However, it is clear that other frequency components are also present in the response of the hook block and the tower, namely 0.15 Hz, 0.21 Hz, and 0.34 Hz.

4.2. Time–frequency analysis

A time–frequency analysis is performed to identify the moments in time when the frequencies of 0.15 Hz, 0.21 Hz and 0.34 Hz were excited. Fig. 11 presents the time–frequency responses of the different motion components measured by the hook sensors. For each time–frequency plot, the corresponding power density spectrum is presented on the left-hand side, while a_x and a_y correspond to the acceleration in the free and restricted plane, respectively (Fig. 6). As discussed in Section 3, these planes are defined by the presence of the active tugger line at the hook block. Note that Ω_z denotes the angular velocity around the z-axis of the hook block.

Figs. 11(d) and 11(e) are obtained by subtracting the translational acceleration component caused by the block rotation, as the sensor was not placed at the block's center of rotation. The acceleration due to rotation $\mathbf{a}_\Omega(t)$ is given by

$$\mathbf{a}_\Omega(t) = \frac{\mathrm{d}}{\mathrm{d}t}\mathbf{L} \times \mathbf{\Omega}(t), \tag{6}$$

in which $\mathbf{L}$ is the vector from the center of rotation of the hook block to the location of the sensor, and $(\times)$ denotes the cross product. In this case, $\mathbf{L} = [-0.90, 0.68, 0.35]^{\mathrm{T}}$ m.

From the figures, it becomes clear that the waves induce translational motions throughout the entire operational time window. The peaks at 0.21 Hz and 0.34 Hz are concentrated at relatively small time intervals, which coincide with the moments when the hook block and the tower are lowered. These lowering operations are indicated by vertical lines in time–frequency plots. As the lowering begin, the wire is paid out relatively quickly compared to the other characteristic dynamics of the suspended system. This sudden acceleration, which can be compared to an impact load, in combination with the restrictions posed by the tugger lines, excites a range of vibration modes (translational and rotational). Comparing Fig. 11(a) with 11(d), and 11(b) with 11(e), it is evident that most of the energy at 0.21 Hz and 0.34 Hz is not present when the rotational component is removed. However, for Lift 1, the acceleration a_y still displays some energy at 0.21 Hz (Fig. 11(e)). This is caused by the action of the active tugger line, as can be seen in Fig. 11(f), where the time–frequency response of the active tugger line is presented. The time–frequency responses for Lift 2 can be found in Appendix B, which show similar behavior as described here for Lift 1.

The remaining energy peak at $f = 0.15$ Hz has a more consistent presence during the first 10 minutes of the time window shown. According to Table 3, this vibration occurs when the second translational natural frequency of the system in the free plane (containing the passive tugger line) is excited. Since the cable length was constant and equal to 60 m (Fig. 8(a)) during this time interval, the wind may have excited the system at this frequency due to vortex shedding from the tower. In the following section, the possibility of vortex-induced vibrations is investigated.

4.3. Vortex-induced vibrations

Flow past cylinders has been extensively described in the literature given the periodic nature of the resulting lift forces. These forces are caused by vortices that shed alternately from each side, which can excite natural modes of mechanical systems, resulting in so-called Vortex-Induced Vibration (VIV) (Williamson and Govardhan, 2004). The vortex shedding frequency is governed by the Reynolds (Re) and Strouhal (St) dimensionless numbers (Kundo et al., 2016), which, for a stationary cylinder, can be determined by using the following expression:

$$f = \frac{\mathrm{St(Re)}U}{D}, \tag{7}$$

in which f represents the vortex shedding frequency in Hz, U the flow velocity in m/s and D the cylinder diameter in m. For the range of Reynolds numbers of interest ($\approx 7 \times 10^5$), the Strouhal number is approximately 0.22.

The average wind speeds for Lift 1 and 2 during the measurement campaign were approximately 2.5 and 4 m/s, respectively, as shown in Fig. 12. Furthermore, the wind direction during the operation was stern-quartering starboard side. During the first 10 min of Lift 1, when motions at 0.15 Hz were excited, a fairly constant wind was present with a speed of approximately 2.5 m/s (Fig. 12(a)). As the speed of the wind gradually increased after 10 min, the intensity of the energy at this frequency decreased. This behavior suggests that the motion with this frequency may be induced by the wind.

To check whether VIV is induced in the system, the average wind speed is compared to the so-called critical velocities of the system. At these velocities, the natural frequency of the system coincides with the

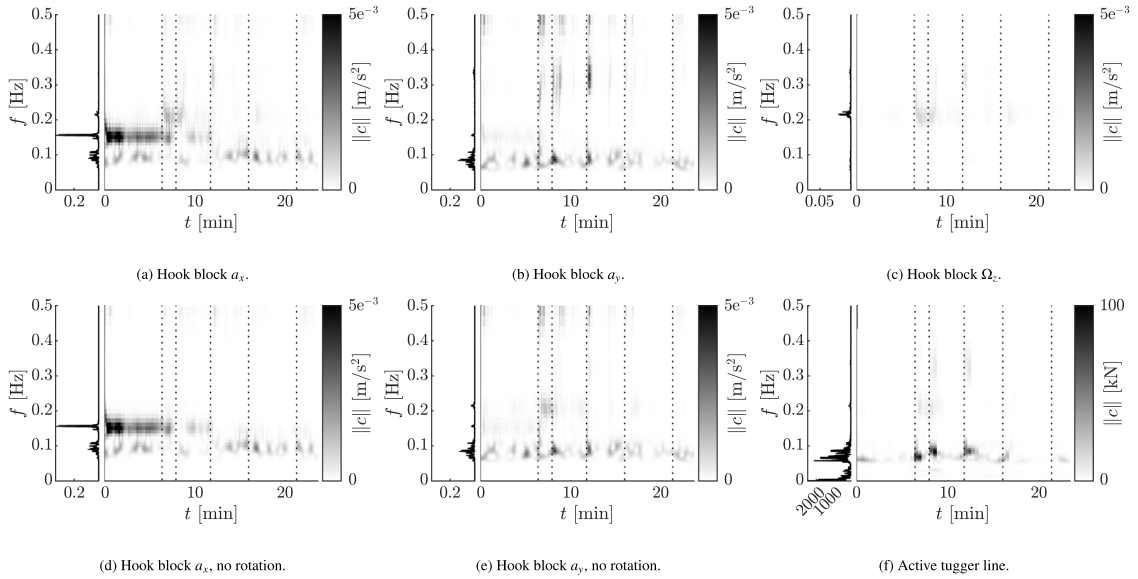

(a) Hook block a_x. (b) Hook block a_y. (c) Hook block Ω_z.

(d) Hook block a_x, no rotation. (e) Hook block a_y, no rotation. (f) Active tugger line.

Fig. 11. Time–frequency plot of the hook block accelerations and angular velocity around its vertical axis, and active tugger tension during Lift 1. The dashed vertical lines denote the moments when the tower was lowered. For each component, the corresponding power density spectrum is presented on the left-hand side.

vortex shedding frequency. Hence, a critical velocity $U_{c,i}$ is given for each natural frequency $f_{n,i}$ by

$$U_{c,i} = \frac{f_{n,i} D}{\mathrm{St}\,(\mathrm{Re})}. \tag{8}$$

For wind speeds around the critical velocity, the vortex shedding frequency will be equal to the natural frequency, *i.e.* frequency lock-in occurs. For a cylinder in air, this lock-in region is a relatively narrow velocity band. However, given the large dimensions and mass of the present structure, no experimental data exist to specify the exact extent of this lock-in region. Therefore, in accordance with Ehrmann et al. (2014), the lock-in region is assumed to be between $0.63U_c$ and $1.4U_c$.

Fig. 12(c) presents the average wind speed divided by the critical velocities for the crane-payload-vessel system (Table 3) during Lift 1. It is clear that for the second mode of vibration the wind speed is close to the critical velocity, and VIV can be generated. When the wind speed increases after $t = 10$ min, it remains within the potential lock-in band (gray shading). Fig. 11 indicates a reduction of VIV earlier than what is predicted in Fig. 12(c). A possible explanation is wind speed estimation errors caused by vessel blockage and atmospheric boundary layer effects. Furthermore, VIV is sensitive to hoisting cable length variations, despite the apparent limited influence of hoisting on the dynamic response of the system (see Fig. 9). For Lift 2, Fig. 12(d) shows that the wind speed is well outside the lock-in region for all three modes of vibration. Therefore, VIV is not expected to occur.

Note that a limitation of this analysis is the high uncertainty in the width of the VIV lock-in region for structures with small relative added mass. Ehrmann et al. (2014) reports locking ranges for systems with m^* (object mass/added mass) up to 67, while the system under consideration is estimated to have $\mathrm{m}^* \approx 245$. Furthermore, the wind measurements were performed on top of the cranes' A-brackets (Fig. 2). They are therefore not necessarily representative of the flow field at the tower's elevation.

4.4. Individual contributions of disturbances to the motion of the tower and block

Fig. 10 presents the power density spectra of the accelerations at the hook block and upper tower. Converting these results to translational displacements is not trivial. Therefore, to compare the impact of each source of disturbance of block and tower motion, the cumulative standard deviation is computed. The motion of the sensors respective to the equilibrium position of the system $\mathbf{u}$ is obtained by the double-time integration of the acceleration:

$$\mathbf{u} = \iint \tilde{\mathbf{a}}\, \mathrm{d}t\, \mathrm{d}t, \tag{9}$$

in which $\tilde{\mathbf{a}}$ is the filtered in-plane acceleration vector, the components of which were filtered using a high-pass filter with $F_c = 0.05$ Hz to eliminate the effect of sensor drift.

From here, the motion spectrum of $\mathbf{u}$ is obtained by computing the Fast Fourier Transform (FFT) in which the two in-plane displacements (u_x and u_y) are treated as a single complex-valued quantity $u = u_x + u_y \mathrm{i}$, resulting in the position frequency spectrum $p(f)$. The power density spectra of $p(f)$ are then given by:

$$S_p(f_i) = \frac{p^2(f_i)}{2\Delta f}, \tag{10}$$

where i represents the ith discrete frequency, and Δf the chosen frequency step in Hz. Finally, the cumulative standard deviation is given by:

$$\sigma_p(f_i) = \sqrt{\int_0^{f_i} S_p(f)\, \mathrm{d}f}. \tag{11}$$

More details on the frequency analysis methodology can be found in Domingos et al. (2023) and Journée et al. (2015). Fig. 13 presents the resulting positional cumulative standard deviation (σ_p), determined from the measured data. The figure reveals that during the floating installation of the wind turbine tower, waves contributed approximately 96% of the block and tower-top motion, while VIV accounted for 3%. Although the effect of hoisting is visible in Figs. 10 and 11, it clearly did not significantly affect the hook block and upper-tower motion during the measurement campaign.

5. Conclusions

The first-ever full-scale measurement campaign for the installation of an offshore wind turbine (OWT) tower using a floating heavy-lift vessel was reported. A series of novel time-synchronized motion tracking modules was developed and placed at strategic positions to capture the dynamic response of the suspended system to environmental disturbances throughout the operation. An analysis of two tower lifts shows that wave disturbances were consistently present during the whole operation and were responsible for about 96% of the hook block and

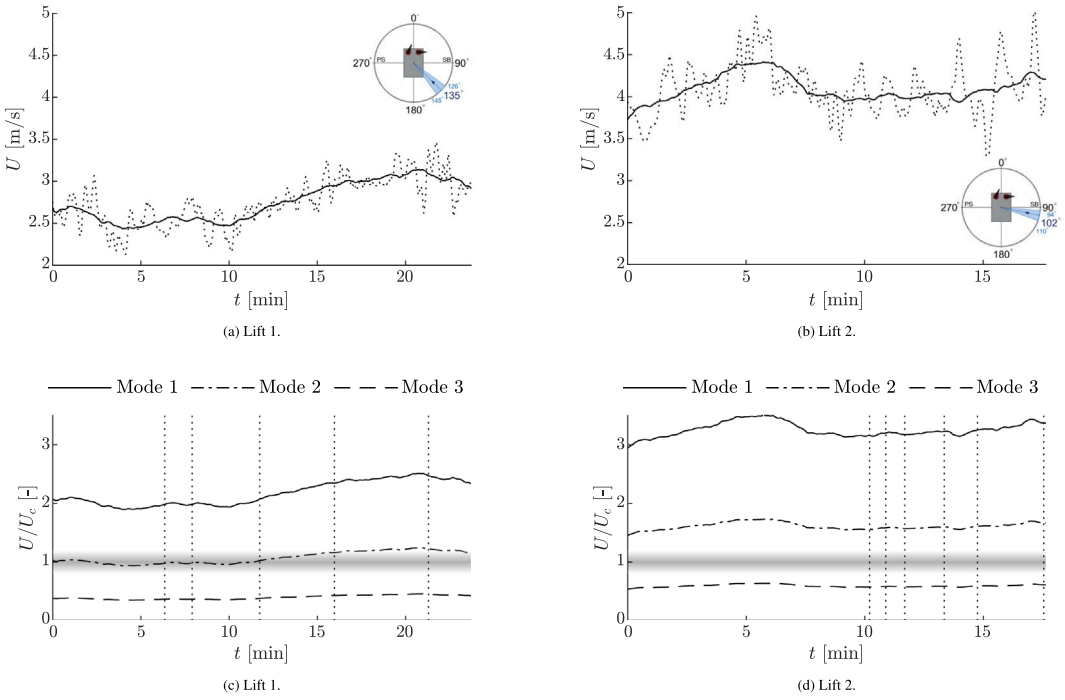

(a) Lift 1. (b) Lift 2.

(c) Lift 1. (d) Lift 2.

Fig. 12. Wind speed and direction during the offshore measurement campaign of Lifts 1 (left) and 2 (right). In the top panels, the measured wind speed is shown in the dotted lines, while the solid lines are the moving averages using a three-minute window. The lower panels present the velocity divided by the mode-dependent critical velocities. The gray band denotes the area where frequency lock-in is possible.

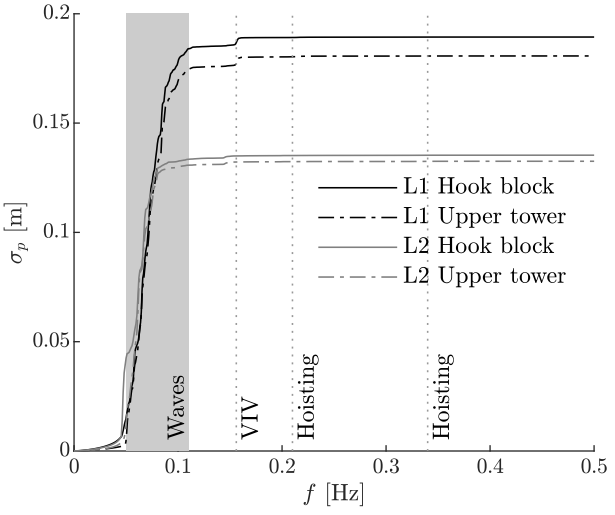

Fig. 13. Cumulative standard deviation spectrum of the hook-block and upper-tower motion during Lift 1 (L1) and Lift 2 (L2).

tower motion, while 3% of the motion is attributed to the presence of an additional passive tugger line, which introduced a natural frequency in the range of wind-driven vortex shedding frequencies, despite the calm environmental conditions. Although the remaining disturbances did not significantly contribute (<1%) to the positional standard deviation of the hook block and tower, a rotational motion of the hook block around its vertical axis is still observed, and its excitation coincides with the hoisting of the payload. According to the data collected, vortex-induced vibration (VIV) is sensitive to hoisting cable length variations, despite the apparent limited influence of hoisting on the dynamic response of the system. Measurements of the tension in the active tugger line, connected to the hook block, show variations in the frequency range of the wave-induced motion, with a small peak at 0.21 Hz, which corresponds to the natural frequency of the block rotation.

The time-synchronized motion tracking modules developed for this campaign succeeded in gathering relevant data in an environment where robustness and versatility are key features. Therefore, their use is advised in future wind turbine installations. In future work, it is recommended to perform an analysis of other phases of the OWT assembly process, so that motion control strategies can be developed for them. Furthermore, conducting measurements in more demanding weather conditions will offer a broader perspective on the floating installation of OWTs, yielding valuable insights for crew training purposes and for improving motion control strategies.

CRediT authorship contribution statement

David Fidalgo Domingos: Writing – review & editing, Writing – original draft, Visualization, Validation, Software, Resources, Project administration, Methodology, Investigation, Formal analysis, Data curation, Conceptualization. **Panagiota Atzampou:** Writing – review & editing, Writing – original draft, Visualization, Validation, Software, Resources, Project administration, Methodology, Investigation, Formal analysis, Data curation, Conceptualization. **Peter Christiaan Meijers:** Writing – review & editing, Writing – original draft, Visualization, Validation, Software, Resources, Methodology, Investigation, Formal analysis, Data curation, Conceptualization. **Sebastião Holbeche Beirão:** Writing – original draft, Software, Resources, Methodology. **Andrei V. Metrikine:** Writing – review & editing, Writing – original draft, Supervision, Resources, Project administration, Investigation, Funding acquisition, Formal analysis, Conceptualization. **Jan-Willem van Wingerden:** Writing – review & editing, Writing – original draft, Supervision, Resources, Project administration, Investigation, Funding acquisition, Formal analysis, Conceptualization. **Peter Wellens:** Writing – review & editing, Writing – original draft, Supervision, Resources, Project administration, Methodology, Investigation, Formal analysis, Conceptualization.

Declaration of competing interest

The authors declare that they have no known competing financial interests or personal relationships that could have appeared to influence the work reported in this paper.

Acknowledgments

This research was part of the project "Floating Offshore Installation of XXL Wind Turbines" (DOT6000-FOX), financially supported by the Netherlands Enterprise Agency (RVO). We are grateful to the members of the Técnico Solar Boat team for designing and assembling the motion-tracking sensors. Rolf van Huffelen, Joris van Drunen, Cris van Popta, and Jesus Rodriguez are acknowledged for their assistance in planning and executing the sensor deployment, as well as for providing essential wind and wave data. We thank the crew members of Delft Offshore Turbine B.V., whose support, even during off-shift hours, has been essential to this research. Lastly, we thank Wim Wien for facilitating access to labs, materials, and tools necessary for assembling and testing the motion sensors.

Appendix A. Numerical model: Governing equations

The triple pendulum shown in Fig. 6 has six degrees of freedom (DOFs), which pertain to the different angles of the pendulum components in the two planes, namely in xz- and yz-plane: the point mass pendulum angle is given by α and β, the sling angle is ζ and ξ, and the angle of rotation of the cylinder around its top point is θ and ϕ in xz- and yz-plane, respectively, as shown in Fig. 6.

The coordinates that describe the motion of the pendulum are given in terms of its three moving components as follows:

$$\mathbf{P}_h(t) = \begin{pmatrix} \ell_h \sin\alpha \\ \ell_h \cos\alpha \sin\beta \end{pmatrix}, \tag{A.1a}$$

$$\mathbf{P}_s(t) = \begin{pmatrix} \ell_s \sin\zeta \\ \ell_s \cos\zeta \sin\xi \end{pmatrix} + \mathbf{P}_h(t), \text{ and} \tag{A.1b}$$

$$\mathbf{P}_L(t) = \begin{pmatrix} L \sin\theta \\ L \cos\theta \sin\phi \end{pmatrix} + \mathbf{P}_s(t), \tag{A.1c}$$

where $\mathbf{P}_L(t)$, $\mathbf{P}_s(t)$ and $\mathbf{P}_h(t)$ are the position vectors of the hanging cylinder, the sling endpoint, and hook mass, respectively. L corresponds to the distance along the longitudinal axis of the cylinder.

The kinetic K and potential U energy of the dynamical system are given by

$$K = \frac{1}{2} M \left\|\dot{\mathbf{P}}_{L,c}(t)\right\|^2 + \frac{1}{2} m \left\|\dot{\mathbf{P}}_h(t)\right\|^2 + T_\omega, \tag{A.2a}$$

$$U = Mg\left(\ell_h + \ell_s + L_c - \hat{\mathbf{k}}\vec{P}_{L,c}(t)\right) + mg\left(\ell_h - \hat{\mathbf{k}}\mathbf{P}_h(t)\right) + \frac{1}{2} k \left\|\cos\gamma\, \hat{\mathbf{i}}\, \mathbf{P}_{L,p}(t)\right\|^2 + \frac{1}{2} k \left\|\sin\gamma\, \hat{\mathbf{j}}\, \mathbf{P}_{L,p}(t)\right\|^2, \tag{A.2b}$$

where $\hat{\mathbf{i}}$, $\hat{\mathbf{j}}$, and $\hat{\mathbf{k}}$ represent the unit vectors of the horizontal x- and y-axis, and the vertical z-axis, respectively. γ is the directional angle of the passive tugger line with respect to the x-axis. $\mathbf{P}_{L,c}(t)$ and $\mathbf{P}_{L,p}(t)$ correspond to the position vectors of two points on the hanging cylinder, namely the endpoint ($L = L_c$) and a point above the center of gravity at $L = 31$ m. T_ω represents the rotational kinetic energy of the hanging load (O'Connor and Habibi, 2013) and can be expressed as

$$T_\omega = \frac{1}{2} I_x(\dot{\phi})^2(\cos\theta)^2 + \frac{1}{2} I_z(\dot{\phi})^2(\sin\theta)^2 + \frac{1}{2} I_y(\dot{\theta})^2, \tag{A.3}$$

where I_x, I_y, and I_z are the moments of inertia of the rotation of the cylinder around its three axes.

For the derivation of the equation of motion, the Lagrangian $\mathcal{L}$ is formulated as follows:

$$\frac{\mathrm{d}}{\mathrm{d}t}\left(\frac{\partial \mathcal{L}}{\partial \dot{\theta}}\right) - \frac{\partial \mathcal{L}}{\partial \theta}, \tag{A.4}$$

where $\mathcal{L} = K - U$. To simplify the simulation of the system, the following assumptions are made: (1) the cable lengths of the hook (ℓ_h) and sling (ℓ_s) are considered as rigid massless elements in the derivation, and (2) the displacements of the hanging components are small compared to the lengths of the pendulum, resulting in the small angle approximation ($\sin\theta \approx \theta$ and $\cos\theta \approx 1$). With assumptions, evaluating Eq. (A.4) gives the following linearized equations of motion (EOMs) of the free vibrations of the dynamical system:

$$\left(\begin{pmatrix} I_{yy} \\ I_{xx} \end{pmatrix} + \frac{ML_c^2}{4}\right)\begin{pmatrix} \ddot{\theta} \\ \ddot{\phi} \end{pmatrix} + \frac{ML_c\ell_h}{2}\begin{pmatrix} \ddot{\alpha} \\ \ddot{\beta} \end{pmatrix} + \frac{ML_c\ell_s}{2}\begin{pmatrix} \ddot{\zeta} \\ \ddot{\xi} \end{pmatrix} + \frac{ML_c}{2} g \begin{pmatrix} \theta \\ \phi \end{pmatrix} + k\ell_p^2 \mathbf{R}\begin{pmatrix} \theta \\ \phi \end{pmatrix} + k\ell_p\ell_h \mathbf{R}\begin{pmatrix} \alpha \\ \beta \end{pmatrix} + k\ell_p\ell_s \mathbf{R}\begin{pmatrix} \zeta \\ \xi \end{pmatrix} = 0, \tag{A.5a}$$

$$(M+m)\ell_h^2\begin{pmatrix} \ddot{\alpha} \\ \ddot{\beta} \end{pmatrix} + M\ell_s\ell_h\begin{pmatrix} \ddot{\zeta} \\ \ddot{\xi} \end{pmatrix} + \frac{ML_c\ell_h}{2}\begin{pmatrix} \ddot{\theta} \\ \ddot{\phi} \end{pmatrix} + (M+m)\ell_h g\begin{pmatrix} \alpha \\ \beta \end{pmatrix} + k\ell_h^2 \mathbf{R}\begin{pmatrix} \alpha \\ \beta \end{pmatrix} + k\ell_p\ell_h \mathbf{R}\begin{pmatrix} \theta \\ \phi \end{pmatrix} + k\ell_s\ell_h \mathbf{R}\begin{pmatrix} \zeta \\ \xi \end{pmatrix} = 0, \tag{A.5b}$$

$$M\ell_s^2\begin{pmatrix} \ddot{\zeta} \\ \ddot{\xi} \end{pmatrix} + M\ell_s\ell_h\begin{pmatrix} \ddot{\alpha} \\ \ddot{\beta} \end{pmatrix} + \frac{ML_c\ell_s}{2}\begin{pmatrix} \ddot{\theta} \\ \ddot{\phi} \end{pmatrix} + M\ell_s g\begin{pmatrix} \zeta \\ \xi \end{pmatrix} + k\ell_s^2 \mathbf{R}\begin{pmatrix} \zeta \\ \xi \end{pmatrix} + k\ell_h\ell s \mathbf{R}\begin{pmatrix} \alpha \\ \beta \end{pmatrix} + k\ell_p\ell_s \mathbf{R}\begin{pmatrix} \theta \\ \phi \end{pmatrix} = 0, \tag{A.5c}$$

where $\mathbf{R}$ is a transformation matrix, given by

$$\mathbf{R} = \begin{pmatrix} \cos^2\gamma & \cos\gamma\sin\gamma \\ \cos\gamma\sin\gamma & \sin^2\gamma \end{pmatrix}. \tag{A.6}$$

Note that geometrically linearizing the EOMs around the equilibrium position leads to the uncoupling of the motion of the triple pendulum in the two separate planes. The resultant of the two planes is the spherical position of the system. In the case of a free suspension ($k = 0$ N/m), the system is fully symmetrical, and, therefore, the problem can be reduced to two identical planar triple pendulums in two perpendicular planes, each with 3 DOFs. However, the additional constraint added to the cylinder by the spring introduces an asymmetry in terms of stiffness and coupling of the planes depending on the orientation of the spring.

The equations of motion can be represented in matrix form as:

$$\mathbf{M}\ddot{x} + \mathbf{K}x = 0, \tag{A.7}$$

where $x = [\theta, \phi, \alpha, \beta, \zeta, \xi]^{\mathrm{T}}$ is the vector of the system's states, and $\mathbf{M}$ and $\mathbf{K}$ are the mass and stiffness matrices, respectively.

The response of the system is assumed to be equal to:

$$x = \bar{X} e^{i\omega_n t}, \tag{A.8}$$

where ω_n represents the natural frequencies of the system which can be determined by solving the eigenvalue problem (Chopra, 2007).

The characteristic equation is given as

$$\det\left\{\left(\mathbf{K} - \omega_n^2 \mathbf{M}\right)\right\} = 0, \tag{A.9}$$

with the non-trivial, real and positive roots of ω_n^2 giving the natural frequencies.

Appendix B. Time–frequency plots

Fig. B.14 presents the time–frequency analysis of the hook block in-plane acceleration and angular velocity together with the active tugger line load for Lift 2. By employing the same procedure as described in Section 4.2 for Lift 1, the acceleration caused by pure rotation of the block is removed from the acceleration signals. Just as for Lift 1, the acceleration peaks at 0.34 Hz are caused solely by block rotation, which in turn is caused by the lowering of the block.

Appendix C. Uncertainty propagation analysis

Fig. C.15 presents the uncertainty in the acceleration power spectra, based on the data in Table 2.

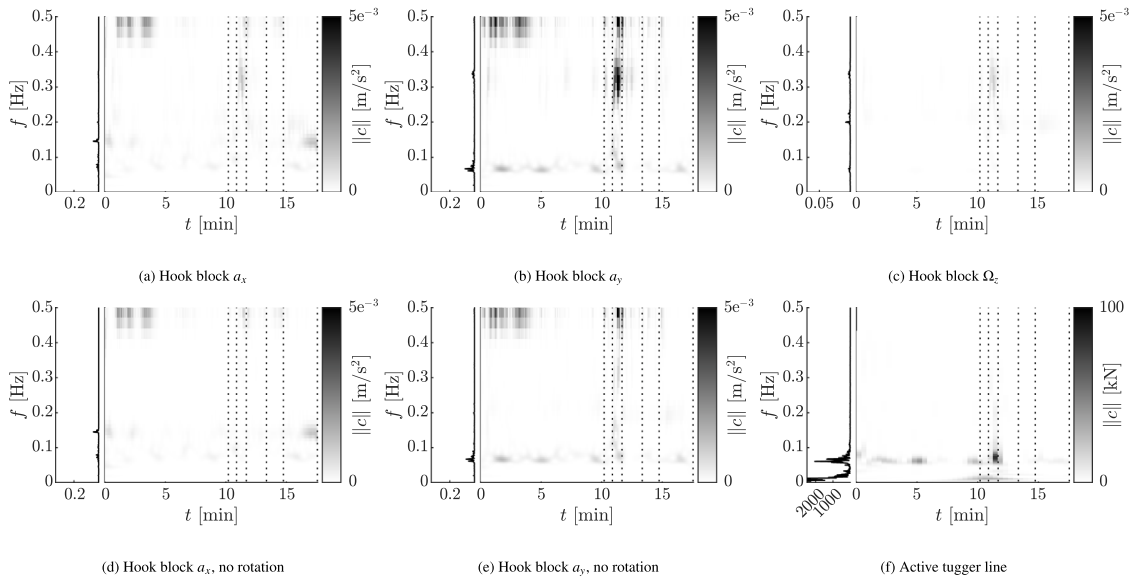

(a) Hook block a_x (b) Hook block a_y (c) Hook block Ω_z

(d) Hook block a_x, no rotation (e) Hook block a_y, no rotation (f) Active tugger line

Fig. B.14. Time–frequency plot of the hook block accelerations and angular velocity around its vertical axis, and active tugger tension during Lift 2. The dashed vertical lines indicate the moments at which the tower was lowered. For each component, the corresponding power density spectrum is presented on the left-hand side.

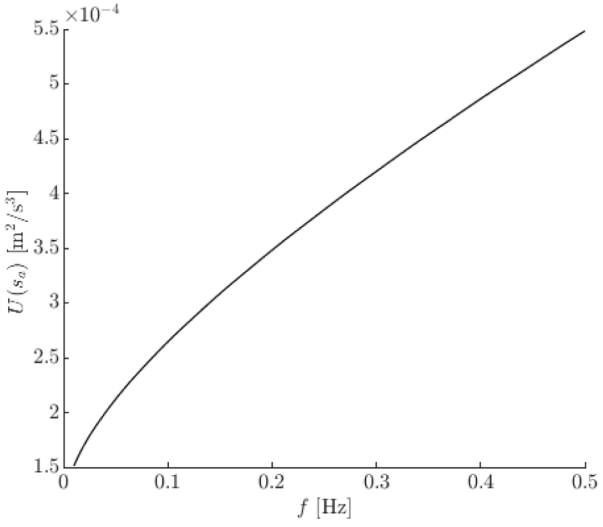

Fig. C.15. Uncertainty of the acceleration power density spectra based on the sensor's specifications, see Table 2.

References

Atzampou, P., Meijers, P.C., Tsouvalas, A., Metrikine, A.V., 2024. Contactless control of suspended loads for offshore installations: Proof of concept using magnetic interaction. J. Sound Vib. 118246.

Bilgili, M., Alphan, H., 2022. Global growth in offshore wind turbine technology. Clean Technol. Environ. Policy 24 (7), 2215–2227.

Cha, J.-H., Roh, M.-I., Lee, K.-Y., 2010. Dynamic response simulation of a heavy cargo suspended by a floating crane based on multibody system dynamics. Ocean Eng. 37 (14–15), 1273–1291.

Chopra, A.K., 2007. Dynamics of Structures. Pearson Education India.

Cis, J., Tojo, F., 2018. A Lipschitz condition along a transversal foliation implies local uniqueness for ODEs. Electron. J. Qualit. Theory Differ. Equat. 1–14. http://dx.doi.org/10.14232/ejqtde.2018.1.13.

de Kruif, B.J., Rossin, B., 2021. Pendulation control for dynamical positioning capable ship; considerations on actuator usage. IFAC-PapersOnLine 54 (16), 120–125.

Díaz, H., Soares, C.G., 2020. Review of the current status, technology and future trends of offshore wind farms. Ocean Eng. 209, 107381.

DOB-Academy, 2022. FOX project video - Offshore Campaign. https://www.youtube.com/watch?v=BGcLoREJI-c.

Domingos, D., Atzampou, P., Meijers, P., Beirão, S., Metrikine, A., van Wingerden, J., Wellens, P., 2024. First floating installation of an OWT tower: Full-scale inertial data. http://dx.doi.org/10.4121/17ae06bb-7da0-4045-ac81-484fa52af13f, 4TU.ResearchData.

Domingos, D., Wellens, P., van Wingerden, J., 2023. Frequency-domain framework for floating installation of wind-turbine towers. Ocean Eng. http://dx.doi.org/10.1016/j.oceaneng.2024.116952.

Ehrmann, R., Loftin, K., Johnson, S., White, E., 2014. Lock-in of elastically mounted airfoils at a 90° angle of attack. J. Fluids Struct. 44, 205–215. http://dx.doi.org/10.1016/j.jfluidstructs.2013.10.008.

Jiang, Z., 2021. Installation of offshore wind turbines: A technical review. Renew. Sustain. Energy Rev. 139, 110576. http://dx.doi.org/10.1016/J.RSER.2020.110576.

Journée, J.M.J., Massie, W.W., Huijsmans, R.H.M., 2015. Offshore Hydromechanics. Delft University of Technology.

Ku, N., Roh, M.-I., 2015. Dynamic response simulation of an offshore wind turbine suspended by a floating crane. Ships Offshore Struct. 10 (6), 621–634. http://dx.doi.org/10.1080/17445302.2014.942504.

Kundo, P., Cohen, I., Dowling, D., 2016. Fluid Mechanics. Elsevier, http://dx.doi.org/10.1016/C2012-0-00611-4.

Larsson, L., 2010. Ship resistance and flow. Published by the Society of Naval Architects and Marine Engineers, SNAME, the Principles of Naval Architecture Series, ISBN: 978-0-939773-76-3.

Meskers, G., van Dijk, R., 2012. A damping tugger system for offshore heavy lifts. In: International Conference on Offshore Mechanics and Arctic Engineering. Vol. 44885, American Society of Mechanical Engineers, pp. 315–323.

O'Connor, W., Habibi, H., 2013. Gantry crane control of a double-pendulum, distributed-mass load, using mechanical wave concepts. Mech. Sci. 4, 251–261. http://dx.doi.org/10.5194/MS-4-251-2013.

Ramirez, L., Fraile, D., Brindley, G., 2019. Offshore Wind in Europe. Tech. rep., WindEurope.

Ren, Z., Verma, A.S., Ataei, B., Halse, K.H., Hildre, H.P., 2021. Model-free anti-swing control of complex-shaped payload with offshore floating cranes and a large number of lift wires. Ocean Eng. 228, 108868. http://dx.doi.org/10.1016/J.OCEANENG.2021.108868.

Williamson, C.H.K., Govardhan, R., 2004. Vortex-induced vibrations. Annu. Rev. Fluid Mech. 36, 413–455. http://dx.doi.org/10.1146/annurev.fluid.36.050802.122128, URL www.annualreviews.org.

WindEurope, 2022. Wind energy in Europe: 2021 statistics and the outlook for 2022–2026.

Zhao, Y., Cheng, Z., Gao, Z., Sandvik, P.C., Moan, T., 2019. Numerical study on the feasibility of offshore single blade installation by floating crane vessels. Mar. Struct. 64, 442–462.